Monthly Notices of the ROYAL ASTRONOMICAL SOCIETY

MNRAS **549,** 1–11 (2026)
Advance Access publication 2026 May 7

https://doi.org/10.1093/mnras/stag854

Distribution functions for spheroids

James Binney ★

Rudolf Peierls Centre for Theoretical Physics, Clarendon Laboratory, Oxford OX1 3PU, UK

Accepted 2026 May 1. Received 2026 April 29; in original form 2026 February 26

ABSTRACT

Galaxy models comprising several components (including dark matter) that are bound by the self-consistently generated gravitational field are readily constructed from distribution functions (DFs) that are analytic functions of the action integrals **J**. We explain why such models have unphysical velocity distributions unless the DFs of hot components satisfy certain conditions as $J_\phi \to 0$. We show how DFs for both isotropic and radially biased spherical systems can be constructed with specified $f(\mathbf{J})$. We show how to construct DFs for flattened systems with significant velocity anisotropy. Construction of self-consistent models rather than populations that are confined by an external potential leads to the conclusion that radially-biased spherical systems are generically unstable to quadrupolar perturbations. Chaos is likely key to maintenance of these constraints during adiabatic disc growth. If the DFs of dark haloes are radially biased, as simulations of cosmic clustering suggest, then models presented here suggest that dark haloes should be significantly oblate.

Key words: Galaxy: kinematics and dynamics – galaxies: elliptical and lenticular, cD – galaxies: haloes – galaxies: kinematics and dynamics.

1 INTRODUCTION

The extent and quality of the data that are available for both our Galaxy and external galaxies has increased enormously in the last few years. In the case of the Milky Way, the *Gaia* data releases (Gaia Collaboration 2018; Gaia Collaboration 2023) and data released by several spectroscopic surveys (M. Steinmetz et al. 2020; L.-C. Deng et al. 2012; Abdurro'uf et al. 2022; S. Buder et al. 2025) have enabled us to study the chemodynamics of our archetypal Galaxy in extraordinary detail. Meanwhile, a new generation of integral field units has dramatically increased our ability to dissect neighbouring galaxies (e.g. Y. Jin et al. 2024; G. Santucci et al. 2024).

Notwithstanding these dramatic observational advances, the available data remain incomplete, are marred by non-negligible uncertainties and influenced by observational biases. The surest way to manage these limitations is to model them with the aid of dynamical models. In its purest form this process involves fitting a model of sufficient sophistication to the data, errors, biases and all.

The more advanced the data are, the more sophisticated must be the models fitted. For example, if the data suffice only to constrain the first three moments of the distribution function (DF), namely the luminosity density, the mean velocity and the velocity dispersion, models constructed from the Jeans equations suffice (e.g. J. J. Binney, R. L. Davies & G. D. Illingworth 1990; P. Li et al. 2023; C. S. Pickett et al. 2025). *Gaia* data yield the full velocity distributions at large numbers of locations, and Jeans modelling cannot adequately interpret such data. Moreover the availability of spectroscopy for huge numbers of stars enables us to probe the dynamics of many different populations within the Milky Way, so models need to furnish predictions for several populations that are confined by a common gravitational potential.

Such models can be constructed in several ways. A popular approach is *N*-body modelling. Unless several million particles are employed, Poisson noise in the gravitational potential is unacceptably large (e.g. M. Aumer, J. Binney & R. Schönrich 2016), so this is inevitably an expensive technique. Moreover, in its standard form the connection between the initial conditions and the final model is opaque, so it is hard to fit a model to given data. Such fits have been achieved by the Made to Measure (M2M) technique (D. Syer & S. Tremaine 1996; F. de Lorenzi et al. 2007) in which the weights of particles are adjusted to optimize the fit to data, but only with a great deal of painstaking labour (e.g. M. Portail et al. 2017).

Another popular, and slightly less labour-intensive approach to galaxy modelling is Schwarzschild's technique (M. Schwarzschild 1979), which has been applied to significant numbers of galaxies in the Sauron (E. Emsellem et al. 2007), CALIFA (S. F. Sánchez et al. 2012), ATLAS 3D (M. e. a. Cappellari 2011), SAMI (J. J. Bryant et al. 2012), and MANGA (K. Bundy et al. 2015) surveys (e.g. R. C. E. van den Bosch et al. 2008; M. Cappellari 2016; L. Zhu et al. 2018, 2022; Y. Jin et al. 2024; G. Santucci et al. 2024).

Here, we develop a third approach to galaxy modelling, $f(\mathbf{J})$ modelling. In this approach, which has been applied to the Milky Way (J. Binney 2010, 2012b, 2018; T. Piffl et al. 2014; T. Piffl, Z. Penoyre & J. Binney 2015; J. Binney & T. Piffl 2015; J. Binney & L. K. Wong 2017; E. Vasiliev 2019b; C. Li & J. Binney 2022a, b; J. Binney & E. Vasiliev 2023, 2024), to dwarf spheroidal galaxies

★ E-mail: Binney@physics.ox.ac.uk

(R. Pascale et al. 2018, 2019, 2024), and to globular clusters (A. Della Croce et al. 2024), one assigns an analytic function of the action integrals to each of a galaxy's components as its DF, and then determines the observables by integrating over velocities. In early work, the galaxy's gravitational potential was assumed up front as in Schwarzschild modelling, but latterly the gravitational potential jointly generated by the components has usually been obtained by solving Poisson's equation. The AGAMA software package (E. Vasiliev 2019a) makes the use of the self-consistently generated potential straightforward and affordable.

Key for the success of $f(\mathbf{J})$ modelling is the availability of a library of functional forms that can be used for the DFs of disc, bulge dark and stellar haloes, etc. Very satisfactory fits to data for the solar neighbourhood were obtained with the 'quasi-isothermal' DF for discs, which was introduced by J. Binney (2010) and refined by J. Binney & P. J. McMillan (2011). J. Binney & E. Vasiliev (2023) proposed an improvement on the quasi-isothermal DF and used it to model the large-scale structure of the Galactic disc.

Disc DFs can plausible vanish as $J_\phi \to 0$ and in this way avoid a problem with current DFs for spheroidal systems, which is the topic of this paper. L. Posti et al. (2015) introduced the 'double-power-law' DF for spheroids, and demonstrated that it can generate L. Hernquist (1990) and NFW (J. F. Navarro, C. S. Frenk & S. D. M. White 1997) components. R. Pascale et al. (2018) introduced the 'exponential' form, which generates dwarf spheroidal galaxies and used it to probe the structure of the dark haloes of these galaxies. Unfortunately, these forms can be safely used only for systems with essentially isotropic velocity distributions. Here, we explain why this is the case and introduce DFs that work also in the case of velocity anisotropy.

It is convenient to break the DF of an axisymmetric model into parts that are even and odd functions of J_ϕ. The odd part determines the rotation of the model but plays no part in determining the density (e.g J. Binney & S. Tremaine 2008). Here, we focus on the even part, which implicitly defines a non-rotating but possibly flattened stellar system.

Section 2 defines the problem to be addressed. Section 3 investigates it analytically. Section 4 solves the problem for spherical systems. Section 5 offers a solution for flattened systems. Section 6 presents self-consistent models rather than components that are confined by an externally generated potential, finding that radial bias in a self-consistent system flattens it even when its DF is $f(J_\mathrm{r}, L)$. Section 6.2 asks whether the conditions on f are still satisfied after the potential has been adiabatically deformed. Section 7 sums up and suggests directions for further work.

2 THE PROBLEM

J. Binney (2014) proposed generating anisotropic models by replacing $H(\mathbf{J})$ as the argument of the DF $f(H)$ of an ergodic model by a similar function of $\mathbf{J}$ in which its components J_i receive different weights: weighting an action more heavily depopulates orbits with large values of that action relative to the ergodic model. For example, decreasing the weighting of J_r induces a radial bias in the model, while weighting J_z more strongly than J_ϕ flattens the model.

L. Posti et al. (2015) showed that DFs that are double power laws in linear combinations of the actions generate self-consistent systems that closely mimic popular spherical system. In particular, the spherical models introduced by L. Hernquist (1990) and J. F. Navarro et al. (1997) are to a good approximation

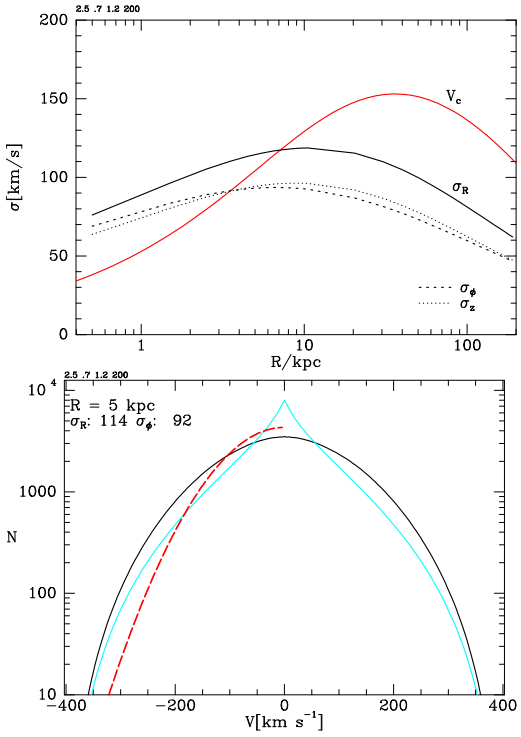

Figure 1. A halo with a DF given by equations (1) and (2) trapped in the potential of a similar body flattened to axis ratio $c/a = 0.5$. The lower panel shows the distributions of v_R in black and v_ϕ in cyan at $(R, z) = (5, 0)$ kpc. The red dashed curve shows the Gaussian with the dispersion of the v_ϕ distribution.

generated by a DF of the form

$$f_1(\mathbf{J}) = \text{constant} \times \frac{(1 + \mathcal{J}_0/\mathcal{J})^\alpha}{(1 + \mathcal{J}/\mathcal{J}_0)^\beta} \mathrm{e}^{-|\mathbf{J}|^2/J_\mathrm{cut}^2}. \tag{1}$$

Here, $\mathcal{J}$ is a linear combination of the actions J_r, J_z, and J_ϕ, the exponent α determines the slope of the model's inner radial density profile, β controls its outer radial density profile, and the constant $\mathcal{J}_0$ determines the radius of the transition between them. Often β is too small to ensure convergence to a finite mass, so equation (1) includes a Gaussian factor to truncate the model at a radius controlled by J_cut. L. Posti et al. (2015) confined their study to spherical systems, which are generated by making the coefficients of J_z and J_ϕ in $\mathcal{J}$ equal, but they pointed out that, by an extension of the B14 proposal, flattened models can be obtained by making the coefficient of J_z larger than that of J_ϕ.

Fig. 1 illustrates the problem with DFs of the type proposed by B14. In the upper panel, the red curve shows the circular speed of the potential well in which a population is trapped. The well is generated by a dark halo with a NFW-like radial profile and axis ratio $c/a = 0.5$. The population has a DF $f_1(\mathcal{J})$ where

$$\mathcal{J} = 0.7J_\mathrm{r} + 1.2J_z + 1.1J_\phi. \tag{2}$$

The black curves in the upper panel show the resulting runs of the principal velocity dispersions, σ_R (full curve), σ_z (dotted curve), and σ_ϕ (dashed curve). These runs are very much what one would expect in a system that has a modest degree of radial bias. The lower panel shows the distributions of v_R in black and v_ϕ in cyan at $(R, z) = (5, 0)$ kpc. The distribution of v_ϕ is sharply peaked. Similarly peaked distributions of v_ϕ are found at other radii. Not only are such peaks incompatible with *Gaia* data for the stellar

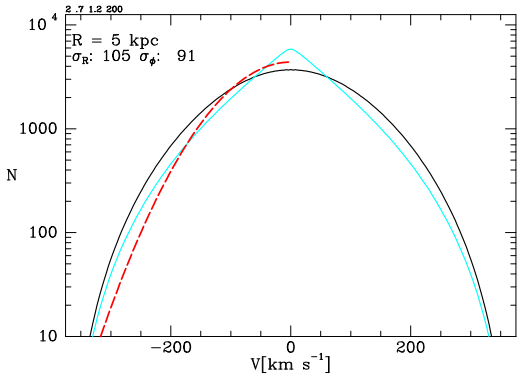

Figure 2. The distributions of radial and azimuthal velocities at $(R, z) = (5, 0)$ kpc when the same population as that shown in Fig. 1 is confined by the equivalent spherical potential.

halo, but in Section 3 it will be shown that a non-zero gradient $\partial N/\partial v_\phi$ at $v_\phi = 0$ violates physical intuition.

Fig. 2 shows the velocity distributions when the same population is trapped in the equivalent spherical well. The v_ϕ distribution is less sharply peaked but is still more peaky than data for the stellar halo permit (e.g. black histograms at top right of fig. 12 in J. Binney & E. Vasiliev 2023 or in the v_ϕ columns of fig. 15 in J. Binney & E. Vasiliev 2024).

3 ANALYTIC CONSIDERATIONS

We now explain why some DFs yield unacceptable distributions of v_ϕ. Consider the velocity distribution $n(\mathbf{v}) = f(\mathbf{x}, \mathbf{v})$ at a given point $\mathbf{x}$ in an ergodic model, i.e. one such that the DF can be written $f(H)$. Then

$$\frac{\partial f}{\partial J_\mathrm{r}} = \frac{\mathrm{d}f}{\mathrm{d}H}\frac{\partial H}{\partial J_\mathrm{r}} = \frac{\mathrm{d}f}{\mathrm{d}H}\Omega_\mathrm{r}, \tag{3}$$

where $\Omega_\mathrm{r}(\mathbf{J})$ is the radial frequency. From the equivalent equations for derivatives wrt J_z and J_ϕ it follows that an ergodic DF satisfies

$$\frac{\partial f/\partial J_\mathrm{r}}{\partial f/\partial J_\phi} = \frac{\Omega_\mathrm{r}}{\Omega_\phi} \quad \text{and} \quad \frac{\partial f/\partial J_z}{\partial f/\partial J_\phi} = \frac{\Omega_z}{\Omega_\phi}. \tag{4}$$

The Hamiltonian $H = \frac{1}{2}v^2 + \Phi$, $f(\mathbf{v})$ is an even function of $\mathbf{v}$, so in the ergodic case $\partial f/\partial v_i \to 0$ as $v_i \to 0$. However, from the perspective of the expression

$$\frac{\partial f}{\partial v_\phi} = \frac{\mathrm{d}f}{\mathrm{d}H}\left(\Omega_\mathrm{r}\frac{\partial J_\mathrm{r}}{\partial v_\phi} + \Omega_z\frac{\partial J_z}{\partial v_\phi} + \Omega_\phi R\right), \tag{5}$$

the vanishing on $\partial f/\partial v_\phi$ is puzzling because $\mathrm{d}f/\mathrm{d}H$ is generically non-zero, and the frequencies only tend to zero as $|\mathbf{J}| \to \infty$. It follows that the last term in the big bracket generates a non-zero value that must be cancelled by the other two terms in the bracket. That is, as $v_\phi \to 0$ at least one of $\partial J_\mathrm{r}/\partial v_\phi$ and $\partial J_z/\partial v_\phi$ must tend to a non-zero value that after weighting by the frequencies magically cancels the last term. (T. Piffl et al. 2015).

T. Piffl et al. (2015) pointed out that taking the argument of f to be a linear combination $\mathcal{J}$ of the actions as proposed by B14 prevents the three terms in the big bracket of equation (5) cancelling, and thus causes $\partial f/\partial v_\phi \neq 0$ at $v_\phi = 0$, which conflicts with both physical intuition and *Gaia* data. The DF needs to be structured such that the three terms do cancel in the limit $v_\phi \to 0$.

Satisfaction of the condition

$$\lim_{v_\phi \to 0}\frac{\partial f}{\partial v_\phi} = 0 \tag{6}$$

actually achieves two things. In addition to ensuring that at any location the distribution in v_ϕ does not have a cusp or dimple at $v_\phi = 0$, it ensures that the distribution of velocity components v_x and v_y parallel to the equatorial plane tends smoothly to isotropy as the symmetry axis is approached – this behaviour is imperative because on the axis all directions perpendicular to the axis are equivalent. Similarly, in a spherical model with a finite central density so the central velocity distribution is well defined, that velocity distribution must be isotropic because all directions are equivalent there.

Isotropy at points on the axis is assured for any $f(\mathbf{J})$ because there the distributions of both v_x and v_y are determined by the dependence of f on a single action (away from the potential's core, the relevant action is J_z, while in the core it is J_r). As the axis is approached, the distributions of the components v_R and v_ϕ in the radial and azimuthal directions should converge on the distribution of v_x. For this to happen, the dependencies of f on J_z [which has control of $f(v_\mathrm{R})$] and on J_ϕ [which dominates $f(v_\phi)$] must converge, and ensuring that f satisfies the condition (6) also imposes this convergence.

3.1 Spherical models

Let v_t be the magnitude of the tangential component of velocity in a spherical system, and ask how $\partial f/\partial v_\mathrm{t}$ contrives to vanish as $v_\mathrm{t} \to 0$ in a spherical model. Any spherical model has a DF that can in principle be expressed as $f(J_\mathrm{r}, L)$, where the total angular momentum is

$$L = rv_\mathrm{t} = J_z + |J_\phi|. \tag{7}$$

In the ergodic case, equation (5) can be written

$$\begin{aligned}\frac{\partial f}{\partial v_\mathrm{t}} &= \frac{\mathrm{d}f}{\mathrm{d}H}\left(\Omega_\mathrm{r}\frac{\partial J_\mathrm{r}}{\partial v_\mathrm{t}} + \Omega_\mathrm{t}\frac{\partial L}{\partial v_\mathrm{t}}\right)\\ &= \frac{\mathrm{d}f}{\mathrm{d}H}\left(\Omega_\mathrm{r}\frac{\partial J_\mathrm{r}}{\partial v_\mathrm{t}} + \Omega_\mathrm{t} r\right).\end{aligned} \tag{8}$$

Differentiating the defining equation of J_r, we have

$$\left.\frac{\partial J_r}{\partial v_\mathrm{t}}\right|_r = \frac{v_\mathrm{t}}{\pi}\int_{r_\mathrm{p}}^{r_\mathrm{a}}\mathrm{d}r'\,\frac{1 - r^2/r'^2}{\sqrt{2(E-\Phi) - L^2/r'^2}}, \tag{9}$$

where $r_\mathrm{p} \le r_\mathrm{a}$ are the roots of the bottom of the integrand. As $v_\mathrm{t} \to 0$, r_p tends to zero and the contribution to the integral from the second term on the top becomes large for any finite r. In fact, the product of the rising integral and the prefactor v_t tends to a non-zero limit. Appendix A shows that

$$\left.\frac{\partial J_\mathrm{r}}{\partial v_\mathrm{t}}\right|_r = -\tfrac{1}{2}r \tag{10}$$

so the two terms in the bracket of equation (8) do cancel provided $\Omega_\mathrm{r} = 2\Omega_\mathrm{t}$.

In the general spherical case, we have

$$\frac{\partial f}{\partial v_\mathrm{t}} = \frac{\partial f}{\partial J_\mathrm{r}}\frac{\partial J_\mathrm{r}}{\partial v_\mathrm{t}} + \frac{\partial f}{\partial L}r. \tag{11}$$

Since $\partial J_\mathrm{r}/\partial v_\mathrm{t}$ is given by equation (10), the terms on the right will cancel as $v_\mathrm{t} \to 0$ iff

$$\lim_{L\to 0}\frac{\partial f/\partial J_\mathrm{r}}{\partial f/\partial L} = 2 = \lim_{L\to 0}\frac{\Omega_\mathrm{t}}{\Omega_\mathrm{r}}. \tag{12}$$

Since the ratio on the right is precisely that appearing in the ergodic relations (4), we conclude that any physically acceptable DF of the form $f(J_\mathrm{r}, L)$ must tend to the ergodic DF as $L \to 0$

This limiting condition achieves two things. In addition to its stated achievement it ensures that as the centre is approached, the velocity distribution in any spherical model tends smoothly to the isotropic central distribution. The latter depends only on the dependence of f on J_r at $L = 0$, while infinitesimally away from the centre the dependence of f on L has a big influence on the distribution of tangential components v_t. A smooth transition to isotropy at the centre is possible only if the structure of the DF for small L is constrained by equation (12).

3.2 Flattened models

Consider now the kinematics of a model with DF $f(\mathbf{J})$ that is confined by a possibly flattened potential. Instead of equation (5) we now have

$$\frac{\partial f}{\partial v_\phi} = \frac{\partial f}{\partial J_\mathrm{r}}\frac{\partial J_\mathrm{r}}{\partial v_\phi} + \frac{\partial f}{\partial J_z}\frac{\partial J_z}{\partial v_\phi} + \frac{\partial f}{\partial J_\phi}R, \tag{13}$$

where (R, z, ϕ) are cylindrical polar coordinates. Consideration of how this equation works as $v_\phi \to 0$ is helped if we return to our analysis of the spherical case with $f(J_\mathrm{r}, L)$ but computing $\partial f/\partial v_\phi$ rather than $\partial f/\partial v_\mathrm{t}$. One easily shows that

(i) $\partial L/\partial v_\phi \to 0$ as $v_\phi \to 0$ at $J_z > 0$ but $\partial L/\partial v_\phi \to \pm R$ when $J_z = 0$;

(ii) the derivative of L behaves thus because in equation (13) the second and third terms on the right usually cancel because

$$\frac{\partial J_z}{\partial v_\phi} = \frac{\partial(L - |J_\phi|)}{\partial v_\phi} = \frac{r^2 v_\phi}{L} \mp R. \tag{14}$$

(iii) $\partial J_\mathrm{r}/\partial v_\phi \to 0$ as $v_\phi \to \pm 0$ at $J_z > 0$ but $\partial J_\mathrm{r}/\partial v_\phi \to \mp R/2$ when $J_z = 0$.

These results suggest that in a flattened potential two different cancellations are required to ensure that $\partial f/\partial v_\phi$ vanishes with v_ϕ. In a spherical model the third term on the right of equation (13) is cancelled by the first term when $J_z = 0$, while in a flattened potential this cancellation occurs for J_z less than a critical value $J_{z\mathrm{crit}}$. In a spherical potential, the second and third terms on the right of equation (13) cancel for $J_z > 0$ because $\partial f/\partial J_z = \partial f/\partial J_\phi$ and $\partial L/\partial v_\phi \to 0$ when $J_z > 0$, while in a flattened potential this cancellation occurs for $J_z > J_{z\mathrm{crit}}$ only.

To understand this situation, it helps to consider orbits in a flattened potential with vanishing J_ϕ (T. Wright & J. Binney 2025). These orbits, which pass over the potential's poles, are conveniently studied in the (x, z) plane (Fig. 3), y being always zero. In this plane a flattened potential is elongated along the x-axis and J_z plays the role of an generalized angular momentum. There is a critical value $J_{z\mathrm{crit}}$ of J_z such that orbits with $J_z > J_{z\mathrm{crit}}$ circulate, while those with $J_z < J_{z\mathrm{crit}}$ librate about the x-axis: one speaks of loop and box orbits. Fig. 3 illustrates this situation by plotting box orbits in blue and loop orbits in red both at vanishing J_ϕ (left panel) and at non-zero J_ϕ (right panel).

When $J_\phi = 0$, the azimuthal coordinate switches from $\phi = 0$ when $x > 0$ to $\phi = \pi$ when $x < 0$. It is not hard to see that on a loop orbit the period of these oscillations in ϕ coincides with the period of the oscillations in both x and z, while on a box orbit the ϕ period equals the period in x but is typically longer than the period in z. That is, when $J_\phi = 0$

$$\Omega_\phi = \begin{cases} \Omega_x = \Omega_z & \text{when } J_z > J_{z\mathrm{crit}} \text{ (loop orbits)} \\ \Omega_x < \Omega_z & \text{when } J_z < J_{z\mathrm{crit}} \text{ (box orbits).} \end{cases} \tag{15}$$

Since $R = |x|$, on box orbits $\Omega_\mathrm{r} = 2\Omega_x$ and $\Omega_\phi = \Omega_\mathrm{r}/2$.

Consider now orbits with non-zero J_ϕ. When $J_\phi \neq 0$ an orbit cannot reach the symmetry axis and it is no longer confined to a plane. When J_ϕ is small we have very anharmonic evolution in ϕ in that it changes slowly until the star approaches the axis, and then ϕ rapidly increases by $\sim\pi$ as the star passes the axis before evolving slowly as the star moves out to apocentre and back. Since the frequencies must be continuous functions on action space, Ω_ϕ must lie close to $\Omega_\mathrm{r}/2$ if J_z is small, and close to Ω_z for larger J_z. That is, the relationship (15) must be approximately valid even for non-zero J_ϕ with $J_{z\mathrm{crit}}$ now identified from the run of orbital frequencies.

Applying these limiting forms of the frequency ratios to the ergodic relations (4), we find that an ergodic DF must be such that

$$\begin{aligned} \frac{\partial f/\partial J_z}{\partial f/\partial J_\phi} &\to 1 \text{ as } J_\phi \to 0 \text{ with } J_z > J_{z\mathrm{crit}} \\ \frac{\partial f/\partial J_r}{\partial f/\partial J_\phi} &\to 2 \text{ as } J_\phi \to 0 \text{ with } J_z < J_{z\mathrm{crit}}. \end{aligned} \tag{16}$$

For these limiting ratios of derivatives in equation to lead to required cancellations in equation (13), we must have that

$$\lim_{v_\phi \to +0} \frac{\partial J_z}{\partial v_\phi} = -\lim_{v_\phi \to +0} \frac{\partial J_\phi}{\partial v_\phi} \quad (J_z > J_{z\mathrm{crit}}) \tag{17}$$

and

$$\lim_{v_\phi \to +0} \frac{\partial J_\mathrm{r}}{\partial v_\phi} = -\tfrac{1}{2}\lim_{v_\phi \to +0} \frac{\partial J_\phi}{\partial v_\phi} \quad (J_z < J_{z\mathrm{crit}}). \tag{18}$$

By considering an ergodic model we have derived relationships, (17) and (18), that are set by the potential alone and can be applied to models with any DF.

Given that the derivatives of $\mathbf{J}$ that appear in equation (13) satisfy equations (17) and (18), it is now clear that the DF of even an anisotropic model must satisfy

$$\lim_{J_\phi \to 0} \frac{\partial f/\partial J_z}{\partial f/\partial J_\phi} = 1 \quad (J_z > J_{z\mathrm{crit}}). \tag{19}$$

and

$$\lim_{J_\phi \to 0} \frac{\partial f/\partial J_\mathrm{r}}{\partial f/\partial J_\phi} = 2 \quad (J_z < J_{z\mathrm{crit}}). \tag{20}$$

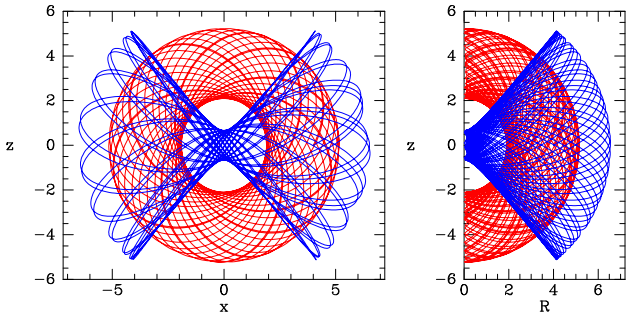

Figure 3. Left panel: two orbits of the same energy in a perfect ellipsoid at $L_z = 0$. The red (loop) orbit has $J_z > J_{z\mathrm{crit}}$ while the blue (box) orbit has $J_z < J_{z\mathrm{crit}}$. Right panel: two orbits that differ from those in the left panel in having small but non-zero L_z and hence must be in the meridional plane.

3.3 Summary

At the beginning of this section we saw that $\partial f/\partial v_\phi$ will not vanish with v_ϕ unless certain products of derivatives of f and of the actions cancel nicely. We further saw that for such cancellation to occur the partial derivatives of f as $J_\phi \to 0$ must satisfy $\partial f/\partial J_\mathrm{r} = \frac{1}{2}\partial f/\partial J_\phi$ at J_z less than a critical value and $\partial f/\partial J_z = \partial f/\partial J_\phi$ at lager J_z. These conditions should ensure that $\partial f/\partial v_\phi$ vanishes by virtue of a relation that we inferred between derivatives of the actions with respect to v_ϕ.

4 DFS FOR SPHERICAL MODELS

We now give an algorithm for defining DFs $f(\mathbf{J})$ that produce acceptable spherical models. Given a point (J_r, L) in reduced action space, we integrate the ODE

$$\frac{\mathrm{d}L}{\mathrm{d}J_\mathrm{r}} = -g(\mathbf{J}), \tag{21}$$

where $g > 0$ is some positive function, in the direction of decreasing J_r and increasing L until $J_\mathrm{r} = 0$ and $L = L_\mathrm{c}$. Then we set the value $f(J_\mathrm{r}, L)$ of the DF at our original point to the value $f_0(L_\mathrm{c})$ taken by a non-negative monotone decreasing function f_0 of one variable. In the case of a dark halo, a suitable choice for f_0 would be

$$f_0(L) = \text{constant} \times \frac{(1+J_0/L)^\alpha}{(1+L/J_0)^\beta}\mathrm{e}^{-L^2/J_\mathrm{cut}^2}, \tag{22}$$

which is the DF defined by equation (1) evaluated on $\mathbf{J} = (0, 0, L)$. If the target were a dwarf spheroidal the exponential DF introduced by R. Pascale et al. (2018) would be our starting point but the procedure would be the same.

With this algorithm, the DF is defined by the functions g and f_0. The path of integration set by g defines a series of orbits of decreasing eccentricity that all have the same phase-space density. The function f_0 says what this density is.

If we set $g = \Omega_\mathrm{r}/\Omega_\mathrm{t}$, the Hamiltonian will be constant along the integration path, and the DF will be that of an ergodic model. If we set $g < \Omega_\mathrm{r}/\Omega_\mathrm{t}$, L will increase more slowly as J_r decreases than in the ergodic case, with the consequence that our final value L_c of L will be smaller than in the ergodic case and the DF $f(J_\mathrm{r}, L) = f_0(L_\mathrm{c})$ will be larger than in the ergodic model. Thus setting $g < \Omega_\mathrm{r}/\Omega_\mathrm{t}$ generates a radially biased model, while setting $g > \Omega_\mathrm{r}/\Omega_\mathrm{t}$ generates a tangentially biased model.

Regardless of what type of model we are generating, g must satisfy $\lim_{L\to 0} g = 2$ so $\partial f/\partial v_\mathrm{t}$ vanishes with v_t.

4.1 Ergodic models

We now use this algorithm to construct an ergodic model of a dark halo. This goal is achieved by setting g to an analytic approximation to $\Omega_\mathrm{r}/\Omega_\mathrm{t}$. We use as our measure of an orbit's circularity

$$c \equiv \frac{L}{L + J_\mathrm{r}}, \tag{23}$$

which ranges from zero for radial orbits to unity for circular orbits. Each curve in Fig. 4 shows $\Omega_\mathrm{t}/\Omega_\mathrm{r}$ as a function of circularity along a sequence of orbits at a given energy. The curves in the lower panel are for orbits confined by a Plummer potential,[1]

[1]The curves produced by an isochrone potential are *extremely* similar.

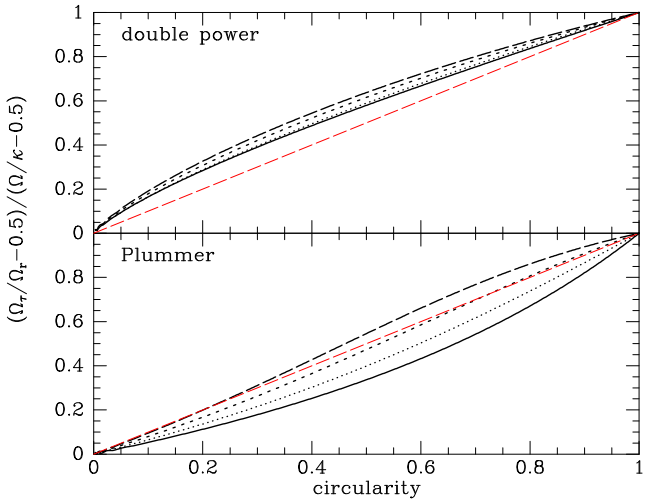

Figure 4. Each black curve shows how $\Omega_\phi/\Omega_\mathrm{r}$ varies with circularity c at a fixed energy in a dark-halo like potential (upper panel) or a Plummer potential (lower panel). The red lines show $y = x$. The potential used for the upper panel is generated by a density distribution with enclosed mass $M = 10$ at $r = 5000$ in which $\rho \propto r^{-1}$ at $r \ll 1$ and $\rho \propto r^{-3}$ at $r \gg 1$. The Plummer model has mass $M = 10$ and unit scale radius.

while those in the upper panel are for orbits confined by a double-power-law potential, similar to that of a baryon-free dark halo. These two potentials differ from one another as much as any two galactic potentials, yet in each case $\Omega_\mathrm{t}/\Omega_\mathrm{r}$ is not far from a linear function of the circularity c, so we have

$$\frac{\Omega_\mathrm{t}}{\Omega_\mathrm{r}} \simeq \tfrac{1}{2} + c\Big(\frac{\Omega}{\kappa} - \tfrac{1}{2}\Big), \tag{24}$$

where Ω and κ are the epicycle frequencies. In the case of the double-power potential, we could refine this approximation by fitting a quadratic or cubic in c to the black curves in the upper panel of Fig. 4, but the examples below indicate that this is unnecessary.

The ratio of epicycle frequencies appearing in equation (24) is evaluated at the energy of the sequence of orbits through which we are integrating. From the potential we can obtain a expression for the ratio in terms of $L_\mathrm{c}(E)$, but $L = L_\mathrm{c}$ is the end-point of the integration. Hence, we are obliged to guess its value. A sensible guess is $L_\mathrm{c} \simeq L + 1.4J_\mathrm{r}$. Fortunately, the DF obtained is extremely insensitive to this guess because the ratio of epicycle frequencies (in contrast to the frequencies themselves) is a weak function of L_c.

The top row of Fig. 5 shows the structure of a population of test particles that have the DF defined by

$$g(\mathbf{J}) = \left[\tfrac{1}{2} + c\Big(\frac{\Omega}{\kappa} - \tfrac{1}{2}\Big)\right]^{-1}, \tag{25}$$

with the constant Ω/κ evaluated at $L_\mathrm{c} = L + 1.4J_\mathrm{r}$ and f_0 given by equation (22) when they are trapped in a spherical double-power-law potential scaled to resemble the potential of our Galaxy's dark halo. Table 1 gives details of the DF. The distributions of v_z and v_ϕ are identical and not distinguishable from the distribution of v_R. In fact, in the top right panel the distribution of v_z at $r = 10$ kpc, plotted in orange, obscures the distributions of v_R and v_ϕ, plotted in black and cyan, respectively. The distributions are remarkably Gaussian: the dashed red curve is the Gaussian with the same standard deviation, $\sigma_\mathrm{R} = 126\,\mathrm{km\,s^{-1}}$, as the actual

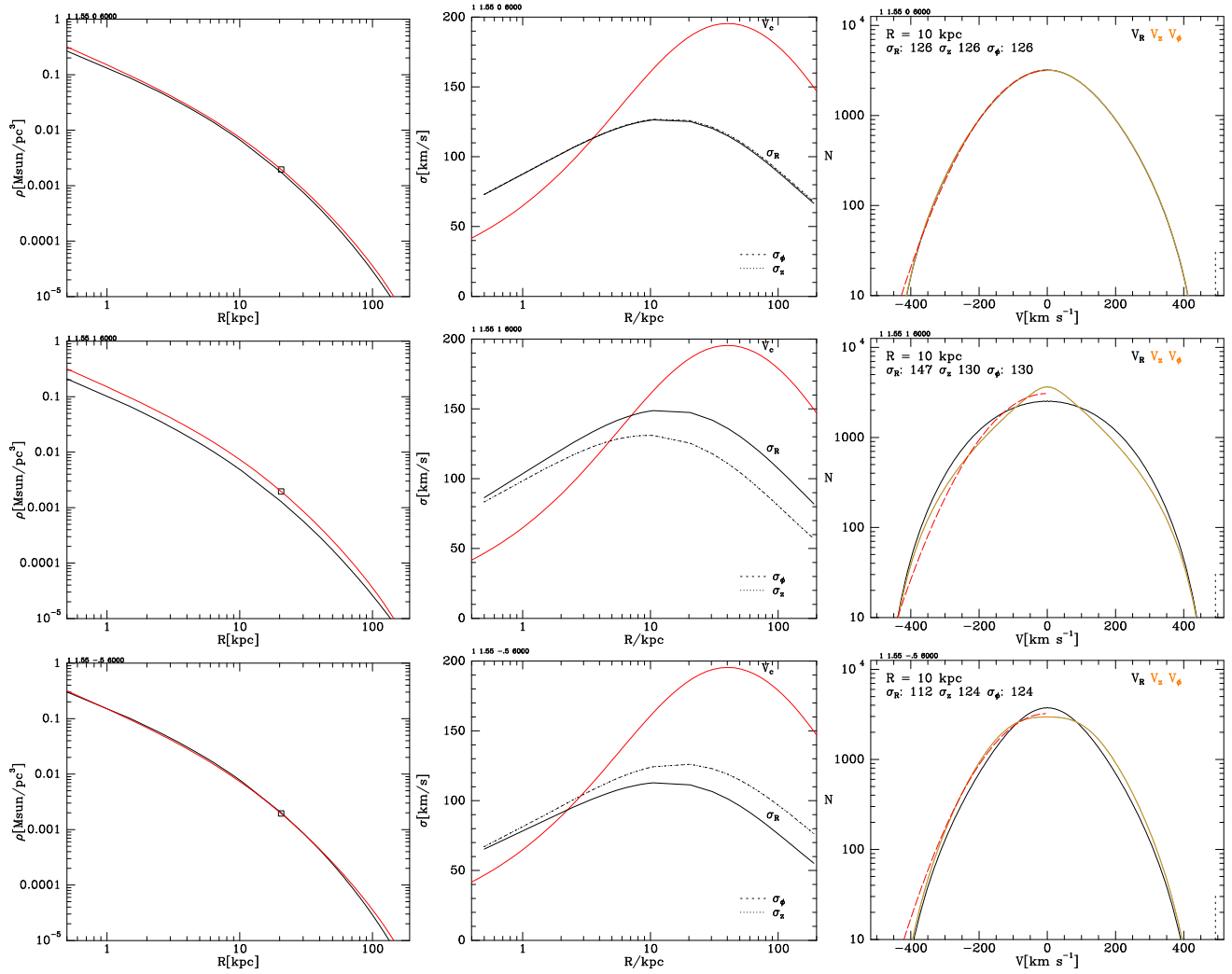

Figure 5. Top row: a population of test particles with DF $f(h_0[\mathbf{J}])$ trapped in a spherical double power-law potential. In the left panel, the red curve shows the density distribution that generates the potential and the black curve shows the density of test particles. The square marks the point at which $\mathrm{d}\ln\rho/\mathrm{d}\ln r = -2$. The middle panel shows the radial and tangential velocity dispersions in this isotropic model. In the right panel, black and overplotted orange curves show the distribution of v_R and v_t velocity components 10 kpc from the centre. The dashed red curve shows the Gaussian with the same standard deviation as $N(v_\mathrm{t})$. Centre row: the same diagnostics for a population of test particles with DF $f(h_2[\mathbf{J}])$ with $\beta_v = 1$ trapped in the same potential. In the right panel, the dashed red curve shows the Gaussian with the same standard deviation as the orange distribution of v_t. Bottom row: as the middle row but for a tangentially biased population with $f(h_1[\mathbf{J}])$ with negative $\beta_v = -0.5$.

Table 1. Parameters of the DFs of the haloes plotted in Figs 5–8. The first three lines relate to Figs 5 and 6 while the fourth line relates to Fig. 7 and 8. Actions are in kpc km s^{-1}.

$M/\,\mathrm{M}_\odot$	J_0	J_cut	α	β	β_v	ϵ
10^{12}	6000	25000	1.55	2.45	0	–
10^{12}	6000	25000	1.55	2.45	1	–
10^{12}	6000	25000	1.55	2.45	−0.5	–
10^{12}	6000	2500	1.53	3	–	200

v_ϕ distribution. The velocity distributions at $R = 50$ kpc plotted in Fig. 6 deviate more from a Gaussian because the truncation of the v distribution at $v_\mathrm{esc} = \sqrt{-2\Phi}$ is more stringent – the dashed vertical line at right bottom of the velocity histograms marks v_esc.

4.2 Introducing velocity anisotropy

As explained above, to generate a radially-biased model we should take $g < \Omega_\mathrm{r}/\Omega_\mathrm{t}$, while continuing to satisfy the constraint $\lim_{L\to 0} g = 2$. A possible choice of g is

$$g_\beta(J_\mathrm{r}, L) = g_\mathrm{H}(J_\mathrm{r}, L)\exp[-\beta_v \sin(c\pi/2)],$$

$$g_\beta(J_\mathrm{r}, L) = g_\mathrm{H}(J_r, L)\exp[-\beta_v \sin(c\pi/2)], \qquad (26)$$

where g_H is given by equation (25). The factor $\exp[-\beta_v \sin(c\pi/2)]$ multiplying g_H causes g to be less than g_H when $\beta_v > 0$ and greater than g_H when $\beta_v < 0$, and thus creates radial/tangential bias depending on the sign of β_v. The sine within the exponential ensures satisfaction of the fundamental requirement that $g \to g_\mathrm{H}$ as $L \to 0$. The choice of a sine is arbitrary: any function that vanishes with its argument and has a finite range might be used.

The centre row of panels in Fig. 5 shows the structure of a population with this DF when $\beta_v = 1$. The left panel of the centre

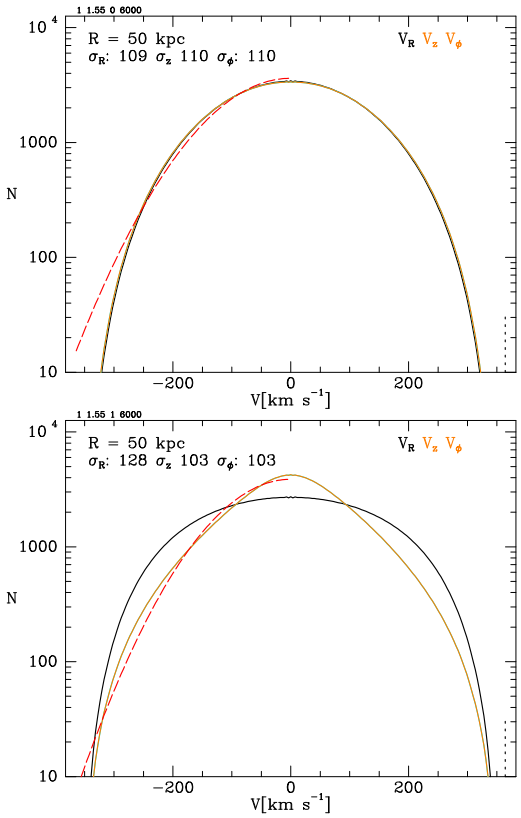

Figure 6. The same as the top right and middle right panels of Fig. 5 but at $r = 50$ kpc. In the ergodic model, the distribution of v_z, plotted in orange, almost completely obscures those of v_R and v_ϕ, plotted in black and cyan. The distributions differ significantly from the Gaussian with the same standard deviation, plotted in broken red. In the radially biased model plotted below, the v_t profile is pointed while that of v_R is very flat-topped.

row shows that moving β_v to a positive value has only a minor impact on the population's radial density profile but the centre panel shows that it causes $\sigma_R > \sigma_t$. The right panel shows that the difference, 147/130 km s^{-1}, in the dispersions at $R = 10$ kpc under-plays the difference between the v_R and v_t velocity distributions. Now both distributions deviate significantly from Gaussians: the shift of orbits towards higher eccentricity has depressed the orange curve for $N(v_t)$ around $v \simeq v_c$ and elevated it around $v_t \sim 0$ by replacing circular orbits with eccentric orbits seen near apocentre. Note that at large $|v|$ the v_R and v_t distributions converge. This is because at high speeds eccentric orbits seen at pericentre boost $N(v_t)$. The lower panel of Fig. 6 shows that at $r = 50$ kpc the differences between the distributions of v_R and v_t are qualitatively the same but quantitatively larger.

The bottom row of panels in Fig. 5 shows a tangentially biased model obtained by setting $\beta_v = -0.5$. The distribution of v_R is now more sharply peaked than that of v_t because negative β_v enhances $N(v_t)$ at $v \sim v_c$ while enhancing $N(v_R)$ at $v \sim 0$ by enhancing the number of circular orbits relative to eccentric orbits.

5 OBLATE MODELS

The strategy used in the last section to obtain anisotropic models of spherical systems is not feasible in the oblate case because it requires a model of the frequency ratios Ω_r/Ω_ϕ and Ω_z/Ω_ϕ as

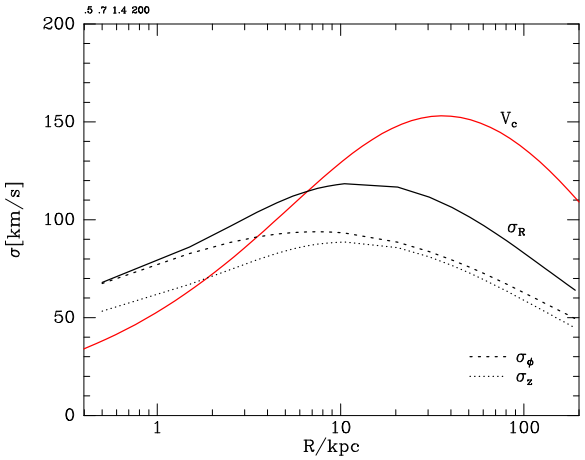

Figure 7. The principal velocity dispersions as functions of radius in a stellar system that is trapped in an NFW potential well. The potential well is generated by a body that has scale length 20 kpc and axis ratio $c/a = 0.5$. Away from the plane $J_\phi = 0$, the DF is a given by equation (1) with $\mathcal{J} = 0.7J_r + 1.4J_z + |J_\phi|$. In equations (27) for the auxiliary DF and (31) for w, the constant $\epsilon = 200$ kpc km s^{-1}.

functions of $\mathbf{J}$, and from Section 3.2 we know that these ratios have a complex dependence on $\mathbf{J}$ near the plane $J_\phi = 0$ (cf. fig 5 of T. Wright & J. Binney 2025). Moreover, an ergodic model cannot generate a flattened gravitational potential – by the virial theorem, flattening requires $\langle v_R^2 \rangle$ to exceed $\langle v_z^2 \rangle$. Consequently, the strategy we pursued in the previous section to obtain anisotropic DFs by modifying an ergodic DF, makes less sense and will not be pursued here.

Given a DF $f(\mathbf{J})$, we define an auxiliary DF $f'(\mathbf{J})$ by

$$f'(\mathbf{J}) \equiv \begin{cases} f(J_r + \frac{1}{2}(|J_\phi| - \epsilon), J_z, \epsilon) & J_z < J_{z\rm crit} \\ f(J_r, J_z + (|J_\phi| - \epsilon), \epsilon) & J_z > J_{z\rm crit}, \end{cases} \tag{27}$$

where ϵ is a small constant with the dimensions of action and the relations $J_{z\rm crit}(J_r)$ and $J_{r\rm crit}(J_z)$ can be computed by the algorithm described by T. Wright & J. Binney (2025) and implemented as the AGAMAb function `getJzcrit`.

The DF (27) satisfies equations (19) and (20). Let $0 \le w(\mathbf{J}) \le 1$ be a weight function such that

$$\lim_{J_\phi \to 0} w(\mathbf{J}) = 1 \text{ and } \lim_{J_\phi \to 0} \nabla_{\mathbf{J}} w = 0, \tag{28}$$

then the DF we use for modelling is

$$f''(\mathbf{J}) = w f'(\mathbf{J}) + (1 - w) f(\mathbf{J}). \tag{29}$$

It's straightforward to show that

$$\lim_{J_\phi \to 0} \nabla_{\mathbf{J}} (f'' - f') = 0 \tag{30}$$

regardless of f, so f'', like f', satisfies equations (19) and (20).

When the confining potential is spherical, the actions can be obtained as functions of $(\mathbf{x}, \mathbf{v})$ from exact formulae. In a flattened potential, exact formulae for J_r and J_z are not available. Here, we obtain J_r and J_z from the Stäckel Fudge (J. Binney 2012a), which involves applying to a general potential formulae that were obtained for a family of potentials with separable Hamilton–Jacobi equations that were identified by Stäckel and extensively explored by T. de Zeeuw (1985). Extensive tests of the Fudge can be found in E. Vasiliev (2019a).

Figs 7 and 8 show profiles of a stellar system that is trapped in the potential well of a body that has the NFW density profile but

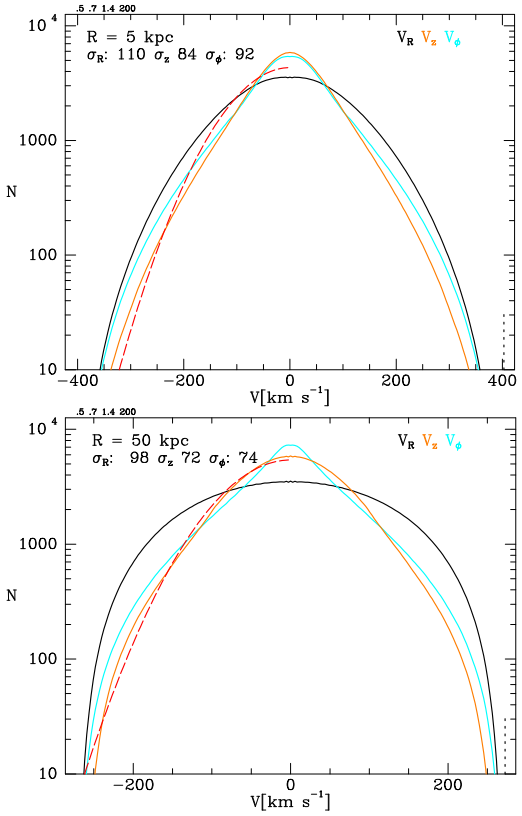

Figure 8. Velocity histograms in the equatorial plane at radii $R = 5$ kpc (upper panel) and $R = 50$ kpc (lower panel) in the model plotted in Fig. 7.

has isodensity surfaces that are similar oblate ellipsoids with axis ratios $c/a = 0.5$. For this figure f in equations (27) and (29) took the form given by equation (1) with $\mathcal{J} = 0.7J_r + 1.4J_z + |J_\phi|$ and J_0, α, β, $J_{\rm cut}$ and ϵ as given in the bottom line of Table 1. Fig. 7 shows in black the principal velocity dispersions at points in the equatorial plane – note that at small radii, σ_ϕ tends to σ_R as it should while σ_z is everywhere smaller. Fig. 8 shows the velocity distributions at points in the equatorial plane at $R = 5$ kpc (upper panel) and $R = 50$ kpc (lower panel). Crucially, none of the histograms has a central cusp. Note that at $R = 50$ kpc the v_z and v_ϕ histograms have quite different shapes even though their second moments are similar.

The weight function used to obtain Figs 7 and 8 was

$$w(\mathbf{J}) = \frac{1}{1 + J_\phi^2/\big[5\epsilon(5\epsilon + J_r + J_z)\big]}, \tag{31}$$

which satisfies equations (28). The model one obtains is not sensitive to the choice of w.

6 SELF-CONSISTENT MODELS

To this point, we have considered populations that are confined by given gravitational potentials. Now we consider models in which the potential is generated by the population itself.

The upper panel of Fig. 9 shows the density $\rho(R, z)$ of a self-consistent halo with a DF constructed on the same principles as the one that generated Fig. 7 and 8. In particular, in equation (1) $\mathcal{J} = 1.4J_r + J_z + |J_\phi|$. The model's velocity distribution is nearly isotropic: at the location of the Sun its velocity dispersions are

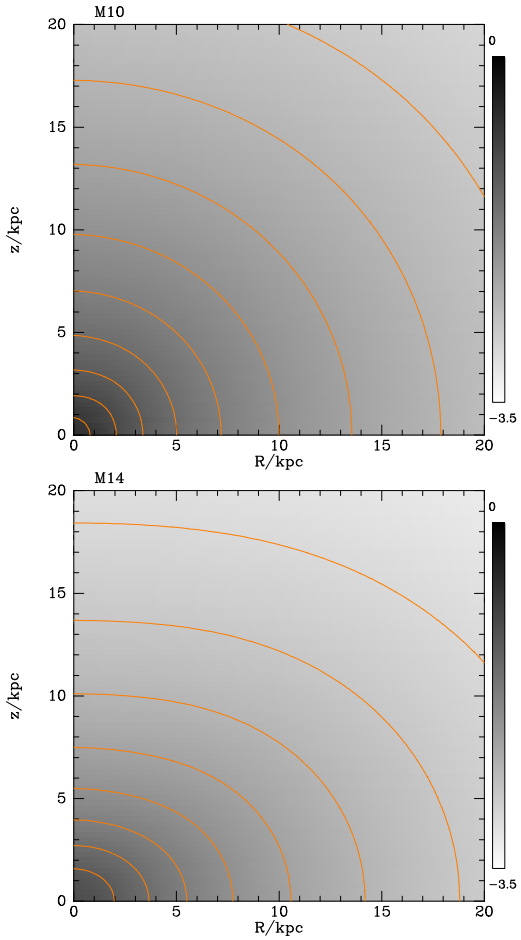

Figure 9. Two self-consistent haloes of mass $10^{12}\,M_\odot$ with DFs given by equations (1), (27), and (31) with $\alpha = 1.6$, $\beta = 2.7$, and $(\mathcal{J}_0, J_{\rm cut}, \epsilon) = (10\,000, 25\,000, 200)$ kpc km s^{-1}. For the upper model the quantity defined by equation (2) is $\mathcal{J} = 1.4J_r + J_z + |J_\phi|$, while for the lower model it is $\mathcal{J} = 0.5J_r + J_z + |J_\phi|$.

$(\sigma_R, \sigma_z, \sigma_\phi) = (152, 150, 146)$ km s^{-1} and its density distribution is very nearly spherical.

The lower panel of Fig. 9 shows the result of reducing the coefficient of J_r in $\mathcal{J}$ from 1.4 to 0.5. This change creates radial bias such that the velocity dispersions at the Sun become $(\sigma_R, \sigma_z, \sigma_\phi) = (134, 100, 102)$ km s^{-1} and the model becomes markedly oblate. Given that the DF depends on $J_z + |J_\phi|$, which, in the case of a spherical potential, corresponds to the total angular momentum L, the oblateness of this model is surprising: the natural expectation is that the model would be spherical but radially biased rather than flattened. Construction of a series of models in which the coefficient of J_r in the definition of $\mathcal{J}$ was gradually increased from 0.5, revealed that the model's axis ratio c/a smoothly moved towards, but never quite reached unity. Fig. 10 shows the axis ratio as a function of radius in the models shown in Fig. 9 and a third model in which the coefficient of J_r is 1.2.

A natural concern is that the oblateness just reported when the DF depends on L is an artefact created by errors in the evaluation of actions by the Stäckel Fudge. The impact of such errors can be assessed by using the same code to construct an isochrone sphere from the analytic DF $f[H(\mathbf{J})]$ that's available for the isochrone. The axis ratio c/a of the resulting model ranged from 1.02 near the

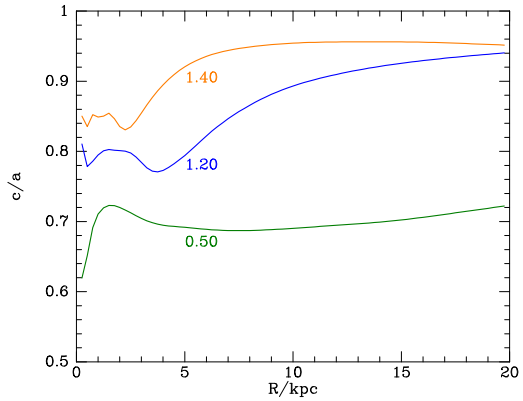

Figure 10. The axis ratio c/a as a function of radius in three self-consistent haloes with DFs based on equation (1). All three DFs depend on J_z and J_ϕ only through $L = J_z + |J_\phi|$. The curves are labelled by the coefficient of J_r in equation (2).

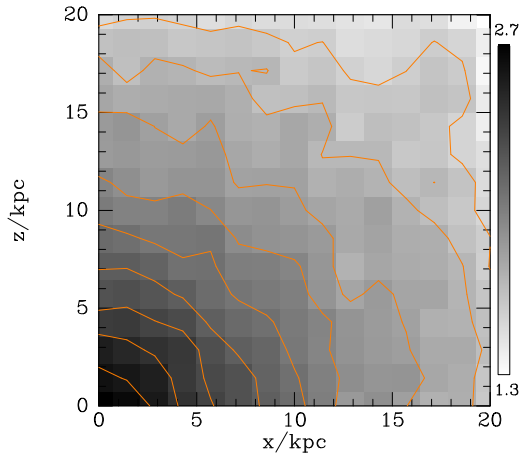

Figure 11. Projected density of an N-body realization of the model shown in the lower panel of Fig. 9. The realization has 100 000 particles and is shown after integration for 3.14 Gyr. The effects of shot noise have been minimized by reflecting particles into the positive quadrant of the xz plane.

centre to 0.98 at 20 kpc. Thus it is very unlikely that the oblateness evident in Fig. 10 is an artefact.

As a further check on the integrity of the model plotted in the lower panel of Fig. 9, we drew from it 100 000 initial conditions for an N-body integration. The tree code YANC (W. Dehnen 2000, 2002) was used to integrate the equations of motion for 3.14 Gyr. YANC determined that in the initial conditions the ratio of kinetic to potential energy, 0.5059 that is very close to the value, 0.5, for a system in equilibrium. Further, plots of density in the meridional plane and the density projected along the y-axis showed no systematic tendency to evolve as the model was integrated – Fig. 11 shows that the system remains oblate to the end of the integration. Unfortunately, shot noise in these plots makes determination of the system's axis ratio problematic.

6.1 Instability of spherical systems

So long as the DF depends on J_z and J_ϕ only in the combination L, a self-consistent spherical model can be constructed for any coefficient of J_r in the definition (2) of $\mathcal{J}$. However, the following argument shows that this model will be unstable whenever it is radially biased by virtue of the coefficient of J_r being less than 1.4.

A. May & J. Binney (1986) imagined transferring the mass of a spherical self-gravitating system to an external body that initially has the same spatial distribution, so the transfer does not alter the distribution of the system's (now massless) stars. When the external body is slowly made slightly non-spherical, the stars respond adiabatically to the changed potential by forming a non-spherical body. If this body is more aspherical than the body that creates the gravitational field, then the original self-consistent model is unstable. They illustrated this principle by exploring prolate distortions of isochrone spheres with Osipkov–Merritt DFs and found that the models remained stable until the anisotropy crossed a non-zero threshold.

J. Goodman (1988) made this argument more secure by showing that when the DF is an even function of velocity, as in the models of Fig. 9, the system is unstable if there is an infinitesimal potential variation $\psi(\mathbf{x})$ and a complex frequency s with $\Re\mathrm{e}\, s > 0$ such that

$$\int \mathrm{d}^3\mathbf{x}\, \psi^* \rho > \int \mathrm{d}^3\mathbf{x}\, \psi^* \widehat{\rho}(s), \tag{32}$$

where $\rho = \nabla^2\psi/(4\pi G)$ is the density required to generate ψ, and $\widehat{\rho}(s)$ is the dynamically induced change in density that occurs when the system is disturbed by the potential $\Phi(\mathbf{x}, t) = \mathrm{e}^{st}\psi(\mathbf{x})$. Bearing in mind that both sides of equation (32) are negative, we see that the system is unstable if the dynamical response causes the system's potential energy to decrease by more than the potential energy associated with the perturbing potential.

The oblate model of Fig. 9 emerged from an initially spherical model by the iterative process by which the potentials of $f(\mathbf{J})$ models are determined (J. Binney 2014). Let $\Phi(\mathbf{x}; \lambda)$ be a one-parameter family of potentials such that $\Phi(\mathbf{x}; 0)$ is the spherical potential from which the iterations started, while $\Phi(\mathbf{x}; 1)$ is the potential after the first iteration, $\Phi(\mathbf{x}; 2)$ is that after two iterations, and so on. Then by the adiabatic principle, successive densities $\rho_i(\mathbf{x})$ for $i = 1, 2, \ldots$ computed during the iteration will coincide with the densities that would arise at stages $\lambda = 0, 1, \ldots$ if we integrated the equations of motion of a very large number of particles in the potential $\Phi(\mathbf{x}; \lambda)$ with λ incrementing very slowly. Notice that at every stage of the evolution, the density obtained from the DF is more flattened than the density that would generate the active potential. It follows that if the equations of motion are integrated in the self-consistent potential, the system will flatten automatically, so the initial, spherical model, is unstable.

This inference suggests that radially biased spherical models are more unstable towards flattening than towards becoming elongated: our experiments suggest that any radial bias, no matter how small, will cause a model to be at least a little bit oblate, whereas previous work (A. M. Fridman & V. L. Polyachenko 1984; P. L. Palmer & J. Papaloizou 1987; J. Barnes, J. Goodman & P. Hut 1986; P. Saha 1991) implies that instability against elongation requires radial bias that exceeds a non-zero threshold. If this result is valid, why was not this discovered before? A. May & J. Binney (1986) did not investigate oblate distortions. Moreover, the models they and other authors investigated differ from the present models in two important respects: (i) the core-envelope profiles of their isochrone models are very unlike the double-power-law radial density profiles of the present models, and (ii) their Osipkov–Merritt DFs create profiles of $\beta = 1 - \sigma_\phi/\sigma_r$ that transition from isotropy ($\beta = 0$) inside a characteristic radius r_a

that moves inwards along their family of DFs, to $\beta \simeq 1$ at radii significantly lager that r_a. The present models have much weaker gradients in $\beta(r)$ (Fig. 7).

6.2 Adiabatic deformation

The realization that the DF of a stellar component is restricted by the potential that it populates raises an interesting issue when the potential is adiabatically deformed. Conventional wisdom (e.g. J. Binney & S. Tremaine 2008, section 4.6.1) is that the function $f(\mathbf{J})$ changes under deformation only to the extent that orbits are resonantly trapped or chaotic. Trapping and chaos are absent in any Stäckel potential, so consider what happens when a perfect ellipsoid is flattened. The flattening increases $J_{z\rm crit}$ at any value of J_r and thus changes the conditions (19) and (20) imposed on a physical DF. Does the DF evolve so it continues to satisfy these conditions, or does it become unphysical?

Consider orbits with vanishing J_ϕ. Then as the potential flattens, the natural value of Ω_z moves upwards, and when $J_{z\rm crit}$ reaches J_z, the link between Ω_ϕ and Ω_z breaks and Ω_z jumps up while Ω_ϕ drops to $\frac{1}{2}\Omega_r$. During the transition, at least one of the frequency differences $\Omega_z - \Omega_\phi$ and $\frac{1}{2}\Omega_r - \Omega_\phi$ must be small and adiabatic conservation of the actions is not assured. Hence it is plausible that the density of stars shifts to either maintain the conditions (16) if they already hold, or moves the DF closer to satisfying them if they do not already hold. It would be interesting to explore this idea by numerically integrating orbits in a slowly deforming Stäckel potential.

7 CONCLUSIONS

Although an axisymmetric model of a stellar system can be derived from any non-negative and normalizable function $f(\mathbf{J})$, the model will be unphysical unless f satisfies the conditions of equation (16). These conditions serve both to ensure that histograms of v_ϕ do not have cusps at $v_\phi = 0$ and to ensure that velocity distribution becomes appropriately symmetric near the centre and near the potential's symmetry axis.

In Section 3, we saw the need for non-trivial cancellations if $\partial f/\partial v_\phi$ is to vanish as $v_\phi \to 0$, and by considering ergodic DFs we showed that these cancellations require the gradients of f with respect to the actions to mirror relations between the fundamental frequencies. Along the way, we established two interesting relations (17) and (18) between derivatives of actions with respect to velocities.

In Section 4, we developed a procedure for generating ergodic DFs for spherical systems and then from these derived anisotropic DFs that satisfy the conditions of equation (16).

In Section 5, we tackled the harder problem posed by flattened systems by defining an auxiliary DF that satisfies the constraints near $J_\phi = 0$, and then defining the DF to be a linear combination of the original and auxiliary DFs that tends to the auxiliary DF as $J_\phi \to 0$. We showed that a component with one of these DFs that resides in an externally generated potential can have physically acceptable kinematics: σ_z is always less that σ_R while σ_ϕ is smaller than σ_R at large radii but tends to σ_R as the centre is approached. Moreover, in these models the v_ϕ distributions do not have cusps at $v_\phi = 0$.

We finished by constructing self-consistent models with DFs that depend on $\mathcal{J} = aJ_r + L$, where a is a free parameter and $L = J_z + |J_\phi|$. When $a \leq 1.4$, the model is radially biased, the bias increasing as a diminishes. To our surprise, all radially biased models proved to be oblate – there appears to be no space for radially biased but spherical models. Concern that this result is an artefact produced by use of the Stäckel Fudge to evaluate actions was allayed by the near sphericity of the isochrone model that the code constructed from the isochrone's known analytic ergodic DF $f(\mathbf{J})$. The validity of the flattened model in which $f(J_r, L)$ was confirmed by initializing an N-body simulation from it.

The oblateness of radially biased models with $f(J_r, L)$ suggests that all radially biased spherical models are unstable to quadrupolar perturbations, but this possibility needs to be confirmed by considering a wider range of density profiles and use of linear-response theory to test for instability.

J. Binney & E. Vasiliev (2023), J. Binney & E. Vasiliev (2024) used the AGAMA software package to fit data from the second and third *Gaia* data releases and the 17 th data release from the APOGEE survey with models in which each of our Galaxy's components is defined by a DF $f(\mathbf{J})$. The DFs of the stellar and dark haloes were chosen such that these components have nearly isotropic velocity distributions in order to avoid the unphysical features described in Section 2. The new DFs open the way to producing much more realistic models of our Galaxy's stellar halo and to tightening constraints on the structure of the dark halo. N-body simulations of the clustering of dark matter strongly suggest that dark haloes are radially biased. From this fact and the results of Section 6 it follows that the dark halo should be quite oblate. Given that the halo's contribution to the circular-speed curve $v_c(R)$ is already tightly constrained and flattening a halo at fixed mass increases v_c, a flatter halo has to be less massive. Stellar streams, large numbers of which have been found in *Gaia* data (R. Ibata et al. 2024), should be able to measure the halo's mass and oblateness with some precision.

ACKNOWLEDGEMENTS

I thank C. Nipoti and R. Pascale for comments on an early draft of this paper, and a referee for constructive criticism of the version submitted.

DATA AVAILABILITY

The computations were performed by C++ code linked to the AGAMAb library (J. Binney, E. Vasiliev & T. Wright 2025), which can be downloaded from `https://github.com/binneyox/AGAMAb`.

REFERENCES

et al., 2022, ApJS, 259, 35
Aumer M., Binney J., Schönrich R., 2016, MNRAS, 459, 3326
Barnes J., Goodman J., Hut P., 1986, ApJ, 300, 112
Binney J., 2010, MNRAS, 401, 2318
Binney J., 2012a, MNRAS, 426, 1324
Binney J., 2012b, MNRAS, 426, 1328
Binney J., 2014, MNRAS, 440, 787
Binney J., 2018, MNRAS, 474, 2706
Binney J., McMillan P. J., 2011, MNRAS, 413, 1889
Binney J., Piffl T., 2015, MNRAS, 454, 3653
Binney J., Tremaine S., 2008, Galactic Dynamics, 2nd edn. Princeton Univ. Press, Princeton, NJ
Binney J., Vasiliev E., 2023, MNRAS, 520, 1832
Binney J., Vasiliev E., 2024, MNRAS, 527, 1915
Binney J., Vasiliev E., Wright T., 2025, preprint (arXiv:2512.06512)
Binney J., Wong L. K., 2017, MNRAS, 467, 2446

Binney J. J., Davies R. L., Illingworth G. D., 1990, ApJ, 361, 78
Bryant J. J. et al., 2012, in McLean I. S., Ramsay S. K., Takami H., eds, Proc. SPIE Conf. Ser. Vol. 8446, Ground-based and Airborne Instrumentation for Astronomy IV. SPIE, Bellingham, p. 84460X
Buder S. et al., 2025, Publ. Astron. Soc. Aust., 42, e051
Bundy K. et al., 2015, ApJ, 798, 7
Cappellari M., 2016, ARA&A, 54, 597
Cappellari M. e. a., 2011, MNRAS, 413, 813
de Lorenzi F., Debattista V. P., Gerhard O., Sambhus N., 2007, MNRAS, 376, 71
de Zeeuw T., 1985, MNRAS, 216, 273
Dehnen W., 2000, ApJL, 536, L39
Dehnen W., 2002, J. Comput. Phys., 179, 27
Della Croce A., Pascale R., Giunchi E., Nipoti C., Cignoni M., Dalessandro E., 2024, A&A, 682, A22
Deng L.-C. et al., 2012, Res. Astron. Astrophys., 12, 735
Emsellem E. et al., 2007, MNRAS, 379, 401
Fridman A. M., Polyachenko V. L., 1984, Physics of Gravitating Systems, Vols I and II. Springer-Verlag, Berlin
Gaia Collaboration, 2018, A&A, 616, A1
Gaia Collaboration, 2023, A&A, 674, A1
Goodman J., 1988, ApJ, 329, 612
Hernquist L., 1990, ApJ, 356, 359
Ibata R. et al., 2024, ApJ, 967, 89
Jin Y., Zhu L., Zibetti S., Costantin L., van de Ven G., Mao S., 2024, A&A, 681, A95
Li C., Binney J., 2022a, MNRAS, 510, 4706
Li C., Binney J., 2022b, MNRAS, 516, 3454
Li P. et al., 2023, A&A, 677, A24
May A., Binney J., 1986, MNRAS, 221, 13P
Navarro J. F., Frenk C. S., White S. D. M., 1997, ApJ, 490, 493
Palmer P. L., Papaloizou J., 1987, MNRAS, 224, 1043
Pascale R., Binney J., Nipoti C., Posti L., 2019, MNRAS, 488, 2423
Pascale R., Nipoti C., Calura F., Della Croce A., 2024, A&A, 684, L19
Pascale R., Posti L., Nipoti C., Binney J., 2018, MNRAS, 480, 927
Pickett C. S. et al., 2025, MNRAS, 540, 1701
Piffl T., Binney J., McMillan P. J. et al., 2014, MNRAS, 445, 3133
Piffl T., Penoyre Z., Binney J., 2015, MNRAS, 451, 639
Portail M., Wegg C., Gerhard O., Ness M., 2017, MNRAS, 470, 1233
Posti L., Binney J., Nipoti C., Ciotti L., 2015, MNRAS, 447, 3060
Saha P., 1991, MNRAS, 248, 494
Sánchez S. F. et al., 2012, A&A, 538, A8
Santucci G. et al., 2024, MNRAS, 534, 502
Schwarzschild M., 1979, ApJ, 232, 236
Steinmetz M. et al., 2020, AJ, 160, 83
Syer D., Tremaine S., 1996, MNRAS, 282, 223
van den Bosch R. C. E., van de Ven G., Verolme E. K., Cappellari M., de Zeeuw P. T., 2008, MNRAS, 385, 647
Vasiliev E., 2019a, MNRAS, 482, 1525
Vasiliev E., 2019b, MNRAS, 484, 2832
Wright T., Binney J., 2025, preprint (arXiv:2512.06519)
Zhu L. et al., 2022, A&A, 664, A115
Zhu L., van de Ven G., Méndez-Abreu J., Obreja A., 2018, MNRAS, 479, 945

APPENDIX A: LIMITING FORM OF $\partial J/\partial v$

Here we infer the limit as $v_t \to 0$ of equation (9).

$$\left.\frac{\partial J_r}{\partial v_t}\right|_r = \frac{v_t}{\pi}\int_{r_p}^{r_a} dr' \, \frac{1 - r^2/r'^2}{\sqrt{2(E-\Phi) - L^2/r'^2}}. \tag{A1}$$

Since the second term in the numerator dominates as r_p tends to zero, we retain only this term. We extract a factor L from the denominator and r^2 from the surviving numerator and change integration variable from r' to $u \equiv 1/r'$. Then we have

$$\left.\frac{\partial J_r}{\partial v_t}\right|_r \simeq -\mathrm{sgn}(v_t)\frac{r}{\pi}\int_{u_a}^{u_p} \frac{du}{\sqrt{a^2 - u^2}}, \tag{A2}$$

where

$$a^2 = 2\frac{E - \Phi(r')}{L^2}. \tag{A3}$$

We neglect the weak u dependence of a since the integral is dominated by the region $u \simeq a \to \infty$ just as the original integral was dominated by the region $r' \simeq r_p \to 0$. Then, with $x = u/a$ the integral tends to

$$\int_0^1 \frac{dx}{\sqrt{1 - x^2}} = \frac{\pi}{2} \tag{A4}$$

and equation (10) follows.

This paper has been typeset from a TEX/LATEX file prepared by the author.